1-15-2019

Thermodynamic and kinetic analysis of the melt spinning process of Fe-6.5 wt.% Si alloy

Senlin Cui
Iowa State University, slcui@iastate.edu

Gaoyuan Ouyang
Iowa State University, gaoyuan@iastate.edu

Tao Ma
Ames Laboratory, taoma@ameslab.gov

Chad R. Macziewski
Iowa State University, chadm@iastate.edu

Valery I. Levitas
Iowa State University and Ames Laboratory, vlevitas@iastate.edu

See next page for additional authors

Thermodynamic and kinetic analysis of the melt spinning process of Fe-6.5 wt.% Si alloy

Abstract

The microstructural evolution of Fe-6.5 wt.% Si alloy during rapid solidification was studied over a quenching rate of 4 × 104 K/s to 8 × 105 K/s. The solidification and solid-state diffusional transformation processes during rapid cooling were analyzed via thermodynamic and kinetic calculations. The Allen-Cahn theory was adapted to model the experimentally measured bcc_B2 antiphase domain sizes under different cooling rates. The model was calibrated based on the experimentally determined bcc_B2 antiphase domain sizes for different wheel speeds and the resulting cooling rates. Good correspondence of the theoretical and experimental data was obtained over the entire experimental range of cooling rates. Along with the asymptotic domain size value at the infinite cooling rates, the developed model represents a reliable extrapolation for the cooling rate > 106 K/s and allows one to optimize the quenching process.

Keywords

Fe-6.5 wt.% Si, Melt spinning, Quenching, Diffusion, Domain growth

Comments

This is a manuscript of an article published as Cui, Senlin, Gaoyuan Ouyang, Tao Ma, Chad R. Macziewski, Valery I. Levitas, Lin Zhou, Matthew J. Kramer, and Jun Cui. "Thermodynamic and kinetic analysis of the melt spinning process of Fe-6.5 wt.% Si alloy." *Journal of Alloys and Compounds* 771 (2018). DOI: 10.1016/j.jallcom.2018.08.293. Posted with permission.

Authors

Senlin Cui, Gaoyuan Ouyang, Tao Ma, Chad R. Macziewski, Valery I. Levitas, Lin Zhou, Matthew J. Kramer, and Jun Cui

Thermodynamic and kinetic analysis of the melt spinning process of Fe-6.5 wt.% Si alloy

Senlin Cui [a], Gaoyuan Ouyang [b], Tao Ma [c], Chad R. Macziewski [b], Valery I. Levitas [a, b, c, d], Lin Zhou [c], Matthew J. Kramer [c], and Jun Cui [b, c]

[a] *Department of Aerospace Engineering, Iowa State University, Ames, Iowa 50011, USA*

[b] *Department of Material Science and Engineering, Iowa State University, Ames, Iowa 50011, USA*

[c] *Ames Laboratory, Department of Energy, Ames, Iowa 50011, USA*

[d] *Department of Mechanical Engineering, Iowa State University, Ames, Iowa 50011, USA*

Corresponding author: vlevitas@iastate.edu (VL), cuisenlin@gmail.com (SC)

Abstract

The microstructural evolution of Fe-6.5 wt.% Si alloy during rapid solidification was studied over a quenching rate of 4×10^4 K/s to 8×10^5 K/s. The solidification and solid-state diffusional transformation processes during rapid cooling were analyzed via thermodynamic and kinetic calculations. The Allen-Cahn theory was adapted to model the experimentally measured bcc_B2 antiphase domain sizes under different cooling rates. The model was calibrated based on the experimentally determined bcc_B2 antiphase domain sizes for different wheel speeds and the resulting cooling rates. Good correspondence of the theoretical and experimental data was obtained over the entire experimental range of cooling rates. Along with the asymptotic domain size value at the infinite cooling rates, the developed model represents a reliable extrapolation for the cooling rate > 10^6 K/s and allows one to optimize the quenching process.

Keywords:
Fe-6.5 wt.% Si, Melt spinning, Quenching, Diffusion, Domain growth

1 Introduction

It is known that Fe-6.5 wt.% Si alloy has optimum electrical and magnetic properties ideally suited for low-mid frequency electricity conversation. Compared to the commonly used 3.2 wt.% Si steel, saturation magnetization decreases by 10% (to 1.7 T) but permeability improves by 27% (to 19,000 at 1 kHz), while electric resistivity improves by 44% (to 82 μΩ-cm) and magnetostriction reduces from 7.8 ppm to 0.1 ppm (a transformer made of 6.5 wt.% Si steel will be silent). However, Fe-6.5 wt.% Si is brittle. The presence of bcc_B2 and/or bcc_$D0_3$ ordered phases is responsible for the materials embrittlement [1]. Due to the low workability, high Si electrical steel sheet can not be manufactured by the conventional hot roll followed by cold roll method. Efforts have been made to mitigate the brittleness issue. Among them, the most commercially successful approach is to diffuse Si into the thin gauge 3.2 wt.% Si steel after chemical deposition. This process was developed in the early 1990s by NKK Steel in Japan. Alternative manufacture methods, preferably using more conventional means, are being intensively pursued worldwide. Hot rolling has been demonstrated to produce thin gauge 6.5 wt.% Si steel sheet because the bcc_B2 phase can be avoided at temperature > 1123 K. Rapid quenching can temporarily suppress the heterogeneous formation of bcc_B2 and bcc_$D0_3$ phases [2]. The delayed formation of Si rich phases even allows a small processing window to perform the traditional cold-roll process. Melt spinning was used to produce 3.8 to 9.3 wt.% silicon steel ribbons by Arai and Tsuya as early as 1980 [3] and by Lin's group in 2015 [4, 5]. The melt-spun thin ribbon can be ductile, as it may be bended 180° without crack [6]. And more recently, the effect of the melt-spin wheel speeds on physical properties of the obtained ribbon was experimentally investitaged by Cui's group [7].

To date, there is no quantative study of the effect of cooling rate on ordering phase transition in Fe-6.5 wt.% Si alloy and corresponding modeling. Melt spinning technique can provide cooling rate up to 10^5-10^7 K/s [8] which is sufficient to systematically study the phase

transitions during rapid cooling of high Si electrical steel. The present work aims to understand the kinetics of the phase transitions during melt spinning of Fe-6.5 wt.% Si alloy by coupling experiments, CALPHAD calculations, and Allen-Cahn macroscopic theory of domain growth.

2 Experiments

Fe-6.5 wt.% Si alloy arc-melted in an argon atomsphere was utilized as raw materials for the melt spinning experiments. Quartz melt spin tubes was fitted with a 0.81 mm precision orifice. 6 g of raw material was inductively melted in the quartz melt spin tubes at about 1863 K in the vacuum chamber partially filed with 1/3 of ultra purity helium. The melt was ejected onto a rotating copper wheel (2.5 cm in width and 25 cm in diameter) under a helium over-pressure of 120 Torr. Experiments were carried out at 3 m/s, 5 m/s, 7 m/s, 10 m/s, 20 m/s, and 30 m/s rotation speeds.

The process was monitored using a number of digital carmera systems. FLIR A8303sc thermal camera with a N_2 filter was used to capture the temperatures of the ribbons surfaces during the melt spinning process through a saphire window. The thermal camera captures the temperatures of the ribbons in the temperature range of 773 K to 1573 K with a resolution of 1920×1080 and a pixel size of 0.7 mm. Thermal profile of the ribbon was obtained by selecting two points along the ribbon and sampling the temperature along the line between them, which was then averaged using multiple frames and converted to temporal temperature profile, i.e. cooling rate, based on the actual distance per pixel and the wheel speed.

The as-spun ribbons were analyzed using transmission electron microscopy (TEM). The specimens were prepared using a FEI Helios NanoLab Dual-beam focused ion beam (FIB) with EasyLift micromanipulator and MultiChem Gas Injection System (MCGIS). The lamellae were lifted out from the wheel side of the ribbons and thinned using Ga ion beam. Samples were observed using a FEI Tecnai G2-F20 TEM equipped with a field emission gun (FEG), under an accelerating voltage of 200 kV. Dark field images of the ordered phases (bcc_B2+bcc_$D0_3$) were obtained using (100) diffraction spots that belongs both to the bcc_B2 and bcc_$D0_3$(200). A

typical TEM dark field image of Fe-6.5 wt.% Si under wheel speed of 30 m/s is shown in Fig. 1, with the selected area electron diffraction pattern shown in the inset. The measurements of the antiphase domain size (r) were carried out using linear intercept method with the help of imageJ software. The red arrowed line in Fig. 1 shows a typical measure of $2r$. The averaged value of all the measured r was taken as the domain size. (It should be noted that (001) spot can not be used to determine the bcc_B2 domain size, if there is a mixture of bcc_B2 and bcc_$D0_3$ phases.) The measured cooling rate and domain size at each wheel speed are listed in Table 1. It is clear from Table 1 that an increase in the cooling rate decreases the domain size. Experiments show that a cooling rate of about 10^6 K/s is necessary to suppress the bcc_B2 domain growth during quenching and obtain the required ductility.

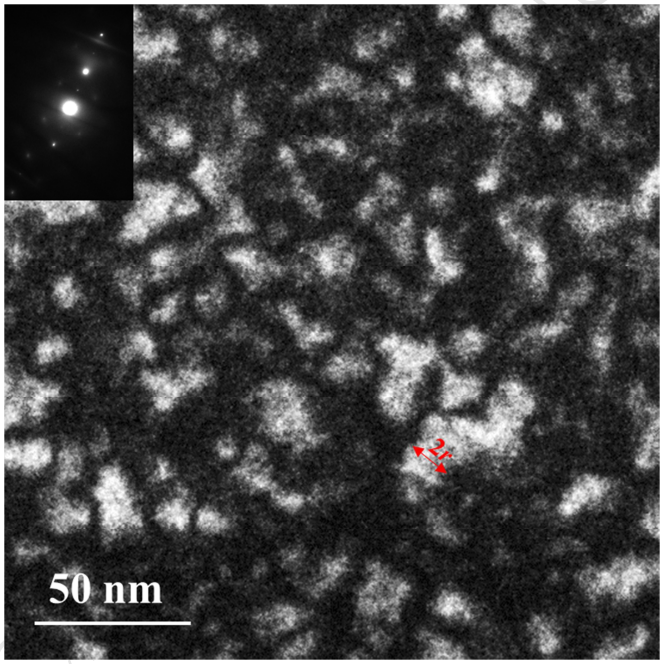

Fig. 1 Dark field TEM image of Fe-6.5 wt.% Si melt spun ribbon at a wheel speed of 30 m/s. The inset is the corresponding selected area electron diffraction pattern, where the B2(100) spot was used for obtaining the dark field image.

Table 1 Summary of cooling rate and bcc_B2 domin size of Fe-6.5 wt.% Si at each wheel speed.

Wheel speed, m/s	Cooling rate, K/s @ 1173 K	Domain Size, nm (Experimental)	Domain Size, nm (Modeling)
3	36200±15500	–	40
5	104900±32900	22±8	22
7	167700±34800	15±3	17
10	349200±33200	10±2	11
20	670600±77100	8±2	7
30	798400±106900	5±2	6

3 Thermodynamic and kinetic analysis

There are two distinct physical cooling periods in the melt spinning process, the wheel-contact period and the free-flight period [9]. In the first stage, the ribbon is in intimate contact with the quench wheel and cooled by the heat conduction across the ribbon-wheel boundary. In the later stage, the ribbon separates from the wheel, and the cooling rate is determined by radiation and convection in the chamber. The first stage thus contains the rapid solidification of the Fe-Si alloy melt and followed by a quench process of the ribbon. The second stage is solely a quenching process. The final microstructure may be a bcc_B2 structure with well-developed or undeveloped antiphase domains, or bcc_B2 and bcc_$D0_3$ mixture depending on the cooling rate [2, 10]. This can also be seen from the Fe-rich Fe-Si phase diagram [11] as shown in Fig. 2. (The phase field of bcc_A2+bcc_B2 shown in Fig. 2 may cannot represent the exact experimental one. However, this will not affect the analysis work within the present paper.) The equilibrium phase of Fe-6.5 wt.% Si at room temperature is bcc_$D0_3$.

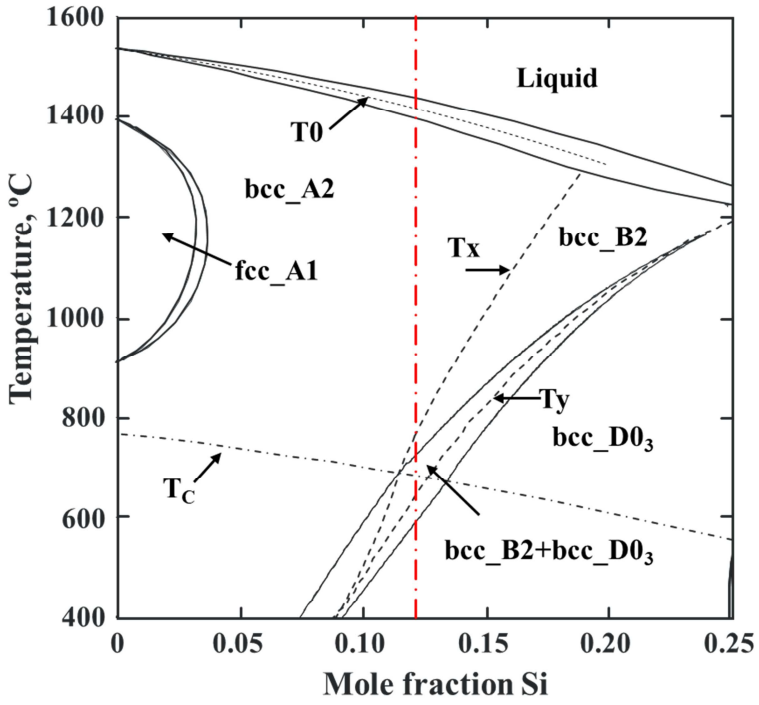

Fig. 2 The Fe-rich Fe-Si phase diagram [11]. The red line indicates the alloy composition of Fe-6.5 wt.% Si. Tx is the bcc_A2/bcc_B2 transition line, Ty is the bcc_B2/bcc_$D0_3$ transition line, T_C is the magnetic transition line, and T0 is the line where liquid and bcc_A2 have equal Gibbs free energy.

3.1 CALPHAD data

The solidification behavior of this alloy was examined using the DICTRA software [12]. To understand the solidification behavior of Fe-6.5 wt.% Si alloy, we need necessary thermodynamic and diffusion mobility data as input. Thermodynamic descriptions for the Fe-Si system are readily available in the literature [11, 13]. In the kinetic part, the atomic mobility parameters of bcc_A2 and liquid were assessed by Wang et al. [14, 15]. However, those for the bcc_B2 and bcc_$D0_3$ phases are unavailable in the literature. As a preliminary work, the atomic mobilities of the bcc_B2 phase were assessed. It is known that the composition dependence of

each atomic mobility parameter for a binary solution expressed in the form of Redlich-Kister polynomial is [16, 17]:

$$\emptyset_i = \sum_p x_p \, \emptyset_i^p + \sum_p \sum_{q>p} x_p x_q \left[\sum_{r=0}^{m} {}^r\emptyset_i^{p,q} \left(x_p - x_q\right)^r\right] \quad (1)$$

where $\emptyset_i$ represents the activation energy $-Q_i$ or the scaled frequency factor $RTlnM_i^0$, $\emptyset_i^p$ is the value of $\emptyset_i$ for element *i* in pure element *p*. ${}^r\emptyset_i^{p,q}$ is the adjustable interaction parameter, and x_p is the mole fraction of element *p*. Helander et al. [18] considered the contribution of chemical ordering (bcc_B2 ordering) on atomic mobility phenomenologically by generalizing the Girifalco model [19]. The activation energy can then be expressed as:

$$Q_i = Q_i^{dis} + Q_i^{ord} \quad (2)$$

where Q_i^{dis} is the contribution from the disordered state and can be expressed as Eq. (1), while Q_i^{ord} presents the contribution from chemical ordering. This quantity is given by an equation in the form:

$$Q_i^{ord} = \sum_p \sum_{q \neq p} Q_i^{p:q} \left[y_p^{\alpha} y_q^{\beta} - x_i x_j\right] \quad (3)$$

where $Q_i^{p:q}$ is a parameter describing the contribution of component *i* due to the chemical ordering of the *p*-*q* atoms on the two sublattices α and β, y_p^{α} is the site fraction of component *p* on the α sublattice. As the atomic mobilities of bcc_A2 and liquid optimized by Wang et al. [14, 15] are compatible with the thermodynamic description by Lacaze and Sundman [13], the ordering contribution of the atomic mobility was also optimized using the thermodynamic factors computed from ref. [13] for consistency. The Q_i^{dis} part was taken from ref. [14] directly. According to ref. [13], the bcc_B2 phase was modeled with a sublattice model $(Fe, Si)_{0.5}(Fe, Si)_{0.5}$, only four ordering parameters were thus optimized for atomic mobilities: $Q_{Si}^{Fe:Si} = Q_{Si}^{Si:Fe} = -62000$ and $Q_{Fe}^{Fe:Si} = Q_{Fe}^{Si:Fe} = -95000$ (all in J/mol). It should be noted that, for simplification, only the experimental interdiffusivities measured by Rabkin et al. [20] and Heikinheimo et al. [21] were considered in the present work. The model-predicted

interdiffusivities at 1006-1483 K are compared with the related experimental data [20, 21] in Fig. 3 with satisfactory agreement. The ordering effect on diffusivity is clearly seen as indicated by the dotted line. Thus, these atomic mobilities are reliable for the subsequent kinetic calculations.

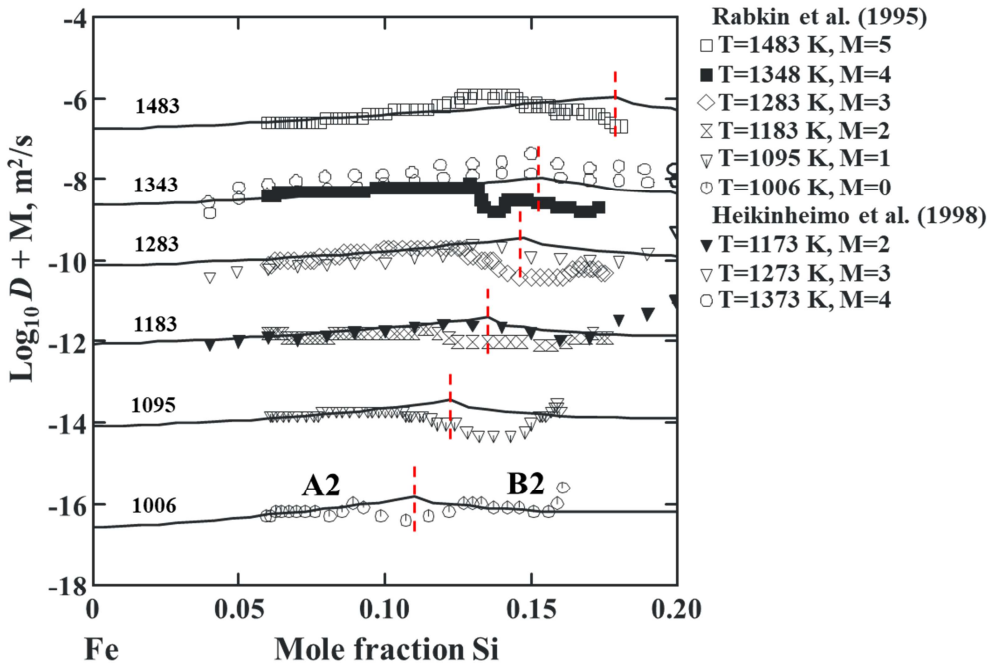

Fig. 3 Model-predicted interdiffusivities (solid lines) of Fe-Si solid solution along with the experimental data (symbols). A constant value of M was added to separate the data.

3.2 Solidification simulation

The bcc_$D0_3$ phase was neglected in the thermodynamic description from Lacaze and Sundman [13]. However, this does not affect the prediction of the bcc_B2 and bcc_$D0_3$ phase formation during solidification, since the liquid composition can be an effective indicator for the ordered phase formation. For example, when the liquid composition reaches 22.67 at.% Si, there will be bcc_B2 formation from liquid under local equilibrium assumption. The bcc_$D0_3$ order contribution to diffusion is thus not necessary and neglected.

In the route of solidification simulation, the temperature of Fe-6.5 wt.% Si was set to the present experimental condition (1863 K). The simulation time was controlled for each cooling rate to ensure complete solidification, i.e. the fraction of solid reaches 1. A double geometry was used in all the solidification simulations. (For more details of double geometry, the readers can refer to DICTRA Manual.) The half of secondary dendrite arm spacing value (λ) should be reasonably used as the length of simulation region. However, λ is difficult to measure in the current melt spinning experiments due to the extreme cooling rate and very thin film produced. Thus, before simulating the experimental cooling rate, the effects of λ and cooling rate on Si concentration in liquid was tested. A series of simulations was carried out at a cooling rate of 10^5 K/s with varying λ from 1.8×10^{-6} m to 1.0×10^{-9} m. The final Si concentration in liquid decreases from 17.76 at.% to 14.53 at.% as λ reduces. In another series of simulations, λ was kept as 2.0×10^{-4} m and the cooling rate was treated as a variable from 1 to 11 K/s. The Si pile up in liquid has a maximum of 17.76 at.% when the cooling rate is 5 K/s in this case. From these two series of simulations, Si concentration in the final liquid is critically related to cooling rate and λ. A smaller λ makes the solute concentration in the final liquid less deviate from the original melt. In other words, it causes smaller segregation. λ is inversely proportional to cooling rate (at least in low cooling rates) and is also composition dependent [22]. Then, the simulations for the real cooling rates measured in the present work were carried out using reasonable λs. The simulated solidification paths at each cooling rate are presented in Fig. 4.

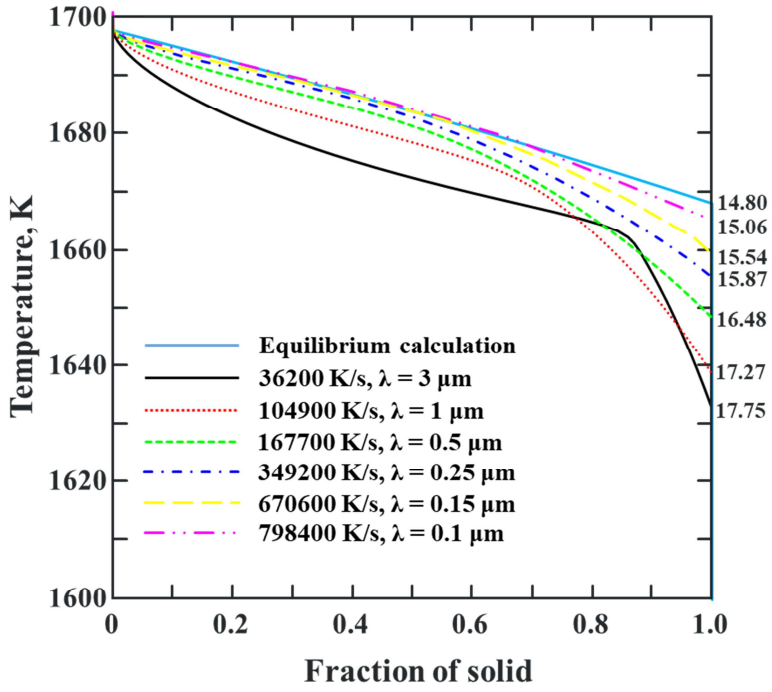

Fig. 4. Simulated solidification paths of Fe-6.5 wt.% Si under different cooling rates and half secondary dendrite arm spacings (λs).

The initial presupposition is that DICTRA is reliable at high cooling rates. The cooling rate, λ, and the final liquid solute concentration in at.% are also indicated in Fig. 4. The equilibrium calculation based on the lever rule is also shown in the figure for reference. The simulation results show that the composition of the final liquid become less and less Si rich (17.75 to 14.80 at.%). So, there is less and less solute redistribution as cooling rate increase. The liquid composition never reaches 22.67 at.% Si at which the bcc_B2 phase starts to form as a primary phase. Thus, it can be concluded that the ordered phase does not form during the solidification process but forms in the subsequent quenching process. The simulation results indicate that there is a certain segregation of the solute element and no solute trapping happens even at the cooling rate of 10^7 K/s. This could be due to that DICTRA calucaltion is based on local equilibrium assumption, solute trapping can seldomly happen. In reallity, when the phase interface mobility reaches the diffusivity of solute in liquid, there will be solute trapping [23]. In

other words, when the liquid is supercooled below the T0 line, the diffusionless phase transition might happen. The micro-composition of Fe-6.5 wt.% Si melt spun should not deviate much from the overall composition according to the above simulation. For example, the simualted time dependent concentration profiles of Fe-6.5 wt.% Si at the cooling rate of 36200 K/s are shown in Fig. 5.

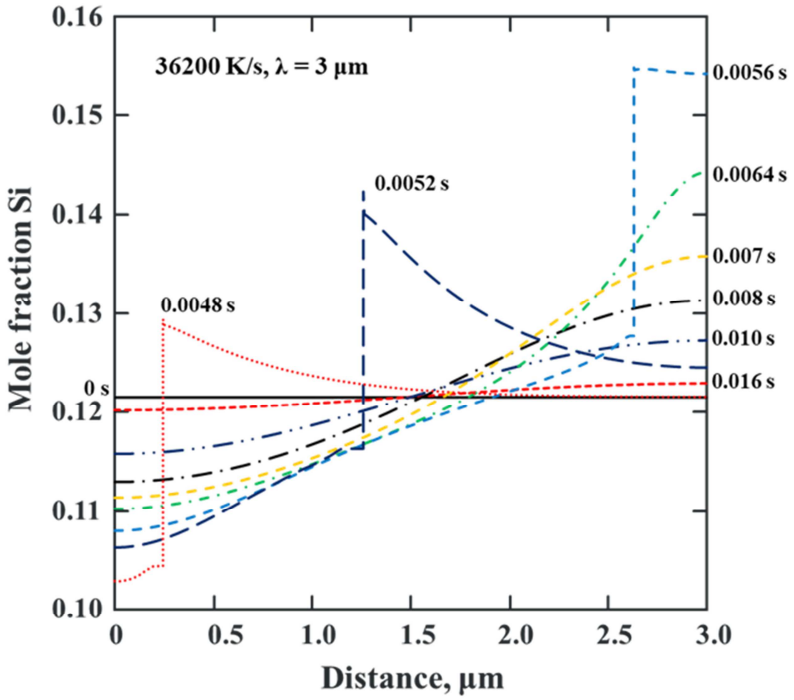

Fig. 5 Simulated time dependent concentration profiles along the half secondary dendrite arm spacing of 3 μm in Fe-6.5 wt.% Si alloy under a cooling rate of 36200 K/s.

Here, solidification only takes about 0.0064 s. Apparent solute pile up in liquid near the propagating solid/liquid interface can be seen from the concentration profiles at time 0.0048 s, 0.0052 s, and 0.0056 s. The Si concentration in primary solid phase also increases with time due to diffusion. The solute concentration in the front and end of the solidification distance has a difference of about 3.4 at.% immediately after solidification complete. However, this difference shrinks quickly in the subsequent quenching process due to high temperature solid state

diffusion, see Fig. 5. The inhomogeneity almost disappears at time 0.016 s when the alloy temperature (1284 K) is above the bcc_A2/bcc_B2 transition temperature. Our simulation results indicate that Fe-6.5 wt.% Si alloy will be even more homogenized at higher cooling rates due to diffusion, and the initial liquid temperature also shows positive correlation with the homogeneity of melt spun.

3.3 Growth of the bcc_B2 antiphase domain

In the subsequent modeling process, the alloy composition was assumed to be unchanged. As indicated by the phase diagram shown in Fig. 2, when the temperature decreases to the bcc_A2/bcc_B2 transition line, the disordered bcc_A2 phase completely loses its stability and the ordered bcc_B2 phase forms through second-order transition. This transition is thus not a classical nuecleation and growth phase change [24]. The microstructure is quite similar to spinodal decompositon, but the order parameter is not consevered. A second-order phase transition is more reasonably described as an antiphase domain growth process [25, 26]. It is known that bcc_B2 has two sublattices $(Fe, Si)_{0.5}(Fe, Si)_{0.5}$ as discussed above. Si may prefer the first or second sublattice, and thus induces two ordered components. As the temperature reached the critical temperature, the long-range-ordering parameter, η, is close to the equilibrium value $\pm\eta_i$ in each domain, but the overall long-range order is still zero [27]. The kinetics of ordering consists of swelling of the web-like regions of both types and an increase in their correlation radii as the boundaries of these regions move in a way that the total volumes of the ordered components is kept the same. In the early work, English [28] studied the bcc_B2 domain growth in Fe-Co-2V alloys using X-ray diffraction and found that the domain size is proportional to $t^{\frac{1}{2}}$. Later, Allen and Cahn [25] developed a microscopic diffusional theory for the antiphase boundary motion. The driving force for the microstructure evolution is related to the curvature of the antiphase boundaries, which reduces during microstructural evolution [25, 26]. According to Allen and Cahn [25], the suface area of the antiphase domain in a unit volume of a specimen, S_v, has the following relationship with the averaged square mean curvature K_m^2 :

$$\frac{dS_v}{dt} = -MK_m^2 S_v \quad (4)$$

where t is time in seconds, M is the coefficient equals to $2\kappa\alpha$, and κ is the gradient energy coefficient, and α is the positive kinetic coefficient in the Allen-Cahn evolution equation. Allen and Cahn in ref. [27] modelled the isothermal domain growth using variable S_v. We intend to model the domain size evolution instead. For bcc_B2 domain growth, Allen and Cahn [25] also derived the following relation: $K_m^2 = \varepsilon {S_v}^2$, where ε is a constant. Considering K_m^2 is inversely proportional to the square of averged domain size r^2, we transform Eq. (4) as:

$$\frac{dr^2}{dt} = k(T) \quad (5)$$

where $k(T)$ is the temperature-dependent coefficient. Then, the isothermal domain size growth follows the parbolic law:

$$[r(t)]^2 - [r(0)]^2 = k(T)t \quad (6)$$

where $r(0)$ is the domain size at $t = 0$. For varying temperature, integral of the Eq. (5) reads:

$$r(t) = \{\, [r(0)]^2 + \int_0^t k(T)dt \,\}^{\frac{1}{2}} \quad (7)$$

To model the continous growth of the aniphase domains during rapid quenching, the kinetic coefficient $k(T)$ can be treated as:

$$k(T) = e^{f(T)} \text{ with } f(T) = a + bT + cTlnT + dT^2 + eT^{-1} \ldots \quad (8)$$

where *a*, *b*, *c*, *d*, and *e* are coefficients to be determined. Depending on the experimental data, one can choose more or less coefficients in Eq. (8).

Time, temperature, and cooling rate ($-\dot{T} > 0$) are correlated during the quenching process. Since the melt spinning process considered in the present work is quite rapid, and due to lack of the detailed modeling of this process, it is reasonable to operate with constant averaged cooling rates depending on rotation speed of the wheel. If we further neglect the incubation time for bcc_A2 to bcc_B2 phase transformation, then $T = T_s + t\dot{T}$, where the transformation

temperature T_s is 1039 K for Fe-6.5 wt.% Si [11]. If the domain growth end temperature is T_f, the total time for domain growth is $t_g = (T_f - T_s)/\dot{T}$. Since exact growth end temperature is unknown and exponential character of the function $k(T)$ can provide vanishning growth rate at low temperature, we consider T_f to be room teperature 298 K.

Radius $r(0)$ is the domain size at critical temperature and it is also the final domain size at infinite cooling rate, when growth is absent. We assume $r(0) = 0.2854$ nm, the lattice parameter of Fe-6.5 wt.% Si at room temperature [29]. In addition, the bcc_$D0_3$ ordered phase formation was neglected due to the technical difficulty in distinguishing it from bcc_B2 and measuring its phase fraction in the melt spinning samples.

Since there are no experimental isothermal domain growth kinetic data in the literature, the model was solely calibrated using the measured cooling rates and domain sizes in the rapidly quenched samples as listed in Table 1. To make an approximation simpler and more practical, we leave just two coefficients, *b* and *e* in function *f* and make *b* linearly dependent on the cooling rate. Thus, $f(T, \dot{T})$ is approximated as:

$$f(T, \dot{T}) = (10^{-9}\dot{T} + 0.0232)T - 10000T^{-1} \quad (9)$$

when $|\dot{T}| > 10^5$ K/s the cooling rate affects function *f*. The simulated domain sizes of bcc_B2 with different cooling rates are shown in Table 1 and Fig. 6.

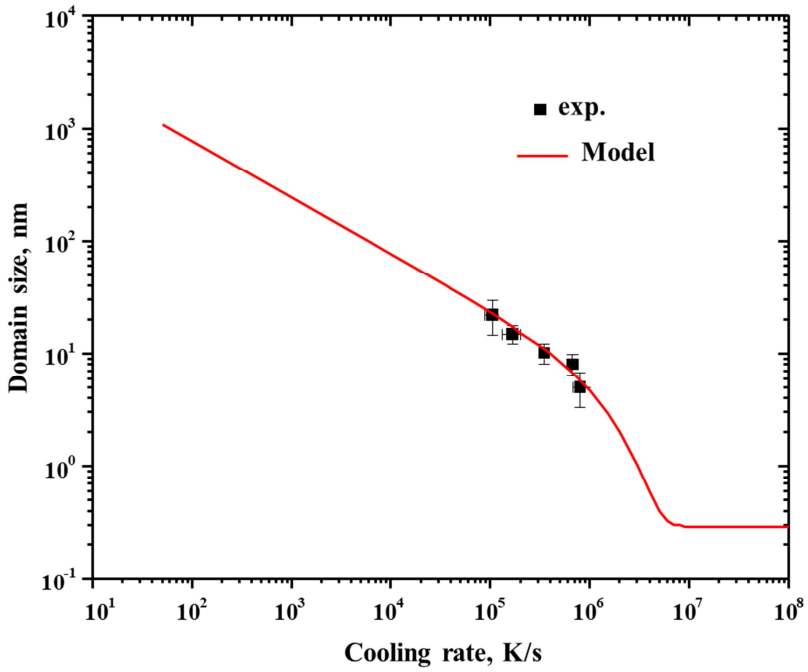

Fig. 6 Model-predicted domain size as a function of cooling rate along with the experimental data.

The experimental data are reasonably reproduced. As the quenching rate increases, the domain size converges to $r(0)$. This happens practically at a cooling rate of 7×10^{6} K/s. Based on the present modeling, the bcc_B2 domain size is comparable with the anti-phase boundary thickness of 2 to 3 nm [30] at a quenching rate of 2 to 3×10^{6} K/s. However, due to slow reduction in the domain size at high cooling rates, a cooling rate of 10^{6} K/s producing domain size of 5 nm would be optimal.

While the model is based on extrapolation of experimental data for higher cooling rate, it is still reliable, because it includes asymptotic value for the infinite cooling rate. It should be noted that the currently obtained function $f\left(T,\dot{T}\right)$ is only reliable for the high cooling rate probably > 1000 K/s.

It is known empirically that the higher the cooling rate is, the higher the ductility of the Fe-6.5 wt.% Si can be reached. We can rationalize this as follows. Ordered bcc_B2 and bcc_$D0_3$ phases are brittle, while disordered bcc_A2 is ductile. Antiphase boundaries between different

bcc_B2 domains cannot be well ordered. Thus, they are similar to the disordered bcc_A2 phase and are ductile. The anti-phase boundary thickness is 2 to 3 nm [30]. Thus, the smaller the size of the bcc_B2 domains is, the larger the volume fraction of the ductile disordered antiphase boundaries will be contained in the material, and the more ductile the resultant multiphase material is. Therefore, a high cooling rate melt spinning can produce Fe-6.5 wt.% Si ribbon with sufficient ductility.

4 Conclusions

Phase transformations during melt spinning of Fe-6.5 wt.% Si electric steel were analyzed using thermodynamic and kinetic calculations and experiments. Rapid solidification cannot be used to quench bcc_A2 as the final phase due to the second-order feature of bcc_A2/bcc_B2 phase transition. There is no bcc_B2 phase formation during the solidification stage over the range of melt spinning conditions studied. No variation is detected in the composition of the melt spun alloys ruling out any solute segregation or inhomogeneity due to high temperature diffusion. The bcc_B2 phase forms during the subsequent quenching process. The domain growth during quenching process was described using the Allen-Cahn theory.

Below, we summarize the main mechanisms of obtaining of Fe-6.5 wt.% Si alloy with sufficient ductility. During the melt spinning process, a constant flow of Fe-6.5 wt.% Si melt was injected on the rotating wheel to produce a continuous ribbon with equal width. Based on the continuity equation, the thickness of the ribbon is inversely proportional to the wheel speed. Because the copper wheel has sufficently high thermal conductivity and is well cooled, the cooling rate increases with the increasing wheel speed. The high cooling rate not only ensures the fine solidification microstructure, but also induces short domain growth time in the solid state. Therefore, the increase in quenching rate decreases the bcc_B2 domain size. Indeed, the bcc_B2 domain growth becomes slow as temperature decreases and even freezes at room temperature. In Fe-6.5 wt.% Si alloy, a cooling rate of about 10^6 K/s is necessary to suppress the bcc_B2 domain growth during quenching and obtain a sufficient ductility. Thus, a high cooling

rate can be used to fabricate an alloy with the required ductility. Its increased ductility can be rationalized in terms of the relatively large volume fraction of ductile disordered antiphase boundaries between various small-size brittle bcc_B2 domains. However, further proof is necessary.

5 Acknowledgments

This work was financially supported by the U.S. Department of Energy, Office of Energy Efficiency and Renewable Energy (EERE) under the Award Number EE0007794. The research was performed at Iowa State University and at Ames Laboratory, which is operated for the U.S. Department of Energy by Iowa State University under the contract number DE-AC02-07CH11358.

6 References

[1] T. Ros-Yañez, Y. Houbaert, O. Fischer, J. Schneider, Production of high silicon steel for electrical applications by thermomechanical processing, J. Mater. Process. Technol, 141 (2003) 132-137.

[2] X. Wang, H. Liu, H. Li, Z. Liu, Effect of cooling rate on order degree of 6.5 wt.% Si electrical steel after annealing treatment, IEEE Trans. Magn., 51 (2015) 2005704.

[3] K. Arai, N. Tsuya, Ribbon-form silicon-iron alloy containing around 6.5 percent silicon, IEEE Trans. Magn., 16 (1980) 126-129.

[4] Y.F. Liang, S. Wang, H. Li, Y.M. Jiang, F. Ye, J.P. Lin, Fabrication of Fe-6.5 wt.% Si ribbons by melt spinning method on large scale, Adv. Mater. Sci. Eng., (2015) 296197.

[5] S. Wan, Y.M. Jiang, Y.F. Liang, F. Ye, J.P. Lin, Magnetic properties and core loss behavior of Fe-6.5 wt.% Si ribbons prepared by melt spinning, Adv. Mater. Sci. Eng., (2015) 410830.

[6] T. Ros-Yanez, Y. Houbaert, O. Fischer, J. Schneider, Production of high silicon steel for electrical applications by thermomechanical processing, J. Mater. Process. Technol, 143-144 (2003) 916-921.

[7] G. Ouyang, B. Jensen, W. Tang, K. Dennis, C. Macziewski, S. Thimmaiah, Y. Liang, J. Cui, Effect of wheel speed on magnetic and mechanical properties of melt spun Fe-6.5 wt.% Si high silicon steel, AIP Advances, 8 (2018) 056111.

[8] E.J. Lavernia, T.S. Srivatsan, The rapid solidification processing of materials: science, principles, technology, advances, and applications, J. Mater. Sci., 45 (2009) 287-325.

[9] M.J. Kramer, H. Mecco, K.W. Dennis, E. Vargonova, R.W. McCallum, R.E. Napolitano, Rapid solidification and metallic glass formation - Experimental and theoretical limits, J. Non-Cryst. Solids, 353 (2007) 3633-3639.

[10] J.S. Shin, J.S. Bae, H.J. Kim, H.M. Lee, T.D. Lee, E.J. Lavernia, Z.H. Lee, Ordering–disordering phenomena and micro-hardness characteristics of B2 phase in Fe–(5–6.5%)Si alloys, Mater. Sci. Eng. A, 407 (2005) 282-290.

[11] S. Cui, I.-H. Jung, Critical reassessment of the Fe-Si system, Calphad, 56 (2017) 108-125.

[12] http://www.thermocalc.com.

[13] J. Lacaze, B. Sundman, An assessment of the Fe-C-Si system, Metall. Trans. A, 22 (1991) 2211-2223.

[14] S. Wang, P. Zhou, W. Zhang, S. Cui, L. Zhang, M. Yin, D. Liu, H. Xu, S. Liu, Y. Du, Atomic mobility and diffusivity of bcc_A2 phase in the Fe–X (X=Cu, Si, Zn) systems, Calphad, 36 (2012) 127-134.

[15] S. Wang, D. Liu, Y. Du, L. Zhang, Q. Chen, A. Engström, Development of an atomic mobility database for liquid phase in multicomponent Al alloys: focusing on binary systems, Int. J. Mater. Res., 104 (2013) 721-735.

[16] B. Jönsson, Assessment of the mobilities of Cr, Fe and Ni in binary fcc Cr-Fe and Cr-Ni alloys, Scand. J. Metall., 24 (1995) 21-27.

[17] J.O. Andersson, J. Ågren, Models for numerical treatment of multicomponent diffusion in simple phases, J. Appl. Phys., 72 (1992) 1350-1355.

[18] T. Helander, J. Ågren, A phenomenological treatment of diffusion in Al–Fe and Al–Ni alloys having B2-b.c.c. ordered structure, Acta Mater., 47 (1999) 1141-1152.

[19] L.A. Girifalco, Vacancy concentration and diffusion in order-disorder alloys, J. Phys. Chem. Solids., 25 (1964) 323-333.

[20] E. Rabkin, B. Straumal, V. Semenov, W. Gust, B. Predel, The influence of an ordering transition on the interdiffusion in Fe-Si alloys, Acta Metall. Mater., 43 (1995) 3075-3083.

[21] E. Heikinheimo, A.A. Kodentsov, F.J.J. van Loo, Interdiffusion in ordered and disordered Fe(Si) solid solution, Scr. Mater., 38 (1998) 1229-1235.

[22] M.Ş. Turhal, T. Savaşkan, Relationships between secondary dendrite arm spacing and mechanical properties of Zn-40Al-Cu alloys, J. Mater. Sci., 38 (2003) 2639-2646.

[23] S.L. Sobolev, Local non-equilibrium diffusion model for solute trapping during rapid solidification, Acta Mater., 60 (2012) 2711-2718.

[24] P.R. Swann, W.R. Duff, R.M. Fisher, Electron metallography of a non-classical order-disorder transition, Phys. Status Solidi, 37 (1970) 577-583.

[25] S.M. Allen, J.W. Cahn, A microscopic theory for antiphase boundary motion and its application to antiphase domain coarsening, Acta Metall., 27 (1979) 1085-1095.

[26] I.M. Lifshits, Kinetics of ordering during phase transitions of the second kind, Zh. Eksp. Teor. Fiz., 42 (1962) 1354-1359.

[27] M.K. Phani, J.L. Lebowitz, Kinetics of an order-disorder transition, Phys. Rev. Lett., 45 (1980) 366-369.

[28] A.T. English, Long-range ordering and domain-coalescence kinetics in Fe-Co-2V, Trans. Metall. Soc. AIME, 236 (1966) 14-18.

[29] F. Lihl, H. Ebel, X-ray examination of the structure of iron-rich alloys of the iron-silicon system, Arch. Eisenhuettenwes., 32 (1961) 489-491.

[30] Y. Murakami, K. Niitsu, T. Tanigaki, R. Kainuma, H.S. Park, D. Shindo, Magnetization amplified by structural disorder within nanometre-scale interface region, Nat. Commun., 5 (2014) 4133.

Table Captions

Table 1 Summary of cooling rate and bcc_B2 domin size of Fe-6.5 wt.% Si at each wheel speed.

Table 1 Summary of cooling rate and bcc_B2 domin size of Fe-6.5 wt.% Si at each wheel speed.

Wheel speed, m/s	Cooling rate, K/s @ 1173 K	Domain Size, nm (Experimental)	Domain Size, nm (Modeling)
3	36200±15500	–	40
5	104900±32900	22±8	22
7	167700±34800	15±3	17
10	349200±33200	10±2	11
20	670600±77100	8±2	7
30	798400±106900	5±2	6

Figure Captions

Fig. 1 Dark field TEM image of Fe-6.5 wt.% Si melt spun ribbon at a wheel speed of 30 m/s. The inset is the corresponding selected area electron diffraction pattern, where the B2(100) spot was used for obtaining the dark field image.

Fig. 2 The Fe-rich Fe-Si phase diagram [11]. The red line indicates the alloy composition of Fe-6.5 wt.% Si. Tx is the bcc_A2/bcc_B2 transition line, Ty is the bcc_B2/bcc_$D0_3$ transition line, T_C is the magnetic transition line, and T0 is the line where liquid and bcc_A2 have equal Gibbs free energy.

Fig. 3 Model-predicted interdiffusivities (solid lines) of Fe-Si solid solution along with the experimental data (symbols). A constant value of M was added to separate the data.

Fig. 4 Simulated solidification paths of Fe-6.5 wt.% Si under different cooling rates and half secondary dendrite arm spacings (λs).

Fig. 5 Simulated time dependent concentration profiles along the half of secondary dendrite arm spacing of 3 μm in Fe-6.5 wt.% Si alloy under a cooling rate of 36200 K/s.

Fig. 6 Model-predicted domain size as a function of cooling rate along with the experimental data.

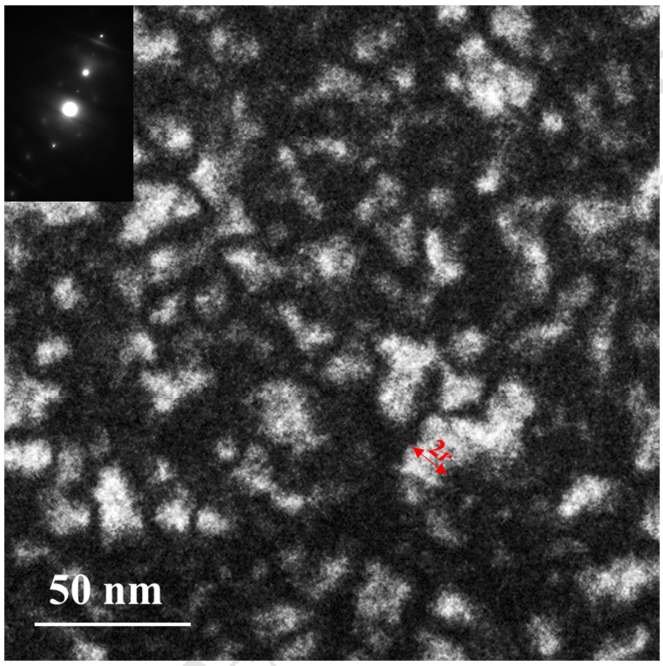

Fig. 1 Dark field TEM image of Fe-6.5 wt.% Si melt spun ribbon at a wheel speed of 30 m/s. The inset is the corresponding selected area electron diffraction pattern, where the B2(100) spot was used for obtaining the dark field image.

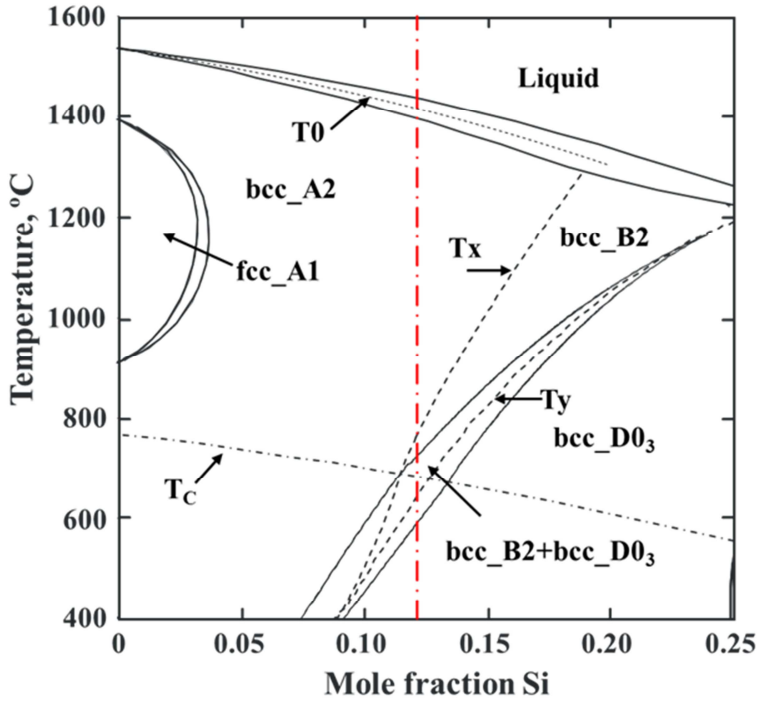

Fig. 2 The Fe-rich Fe-Si phase diagram [11]. The red line indicates the alloy composition of Fe-6.5 wt.% Si. Tx is the bcc_A2/bcc_B2 transition line, Ty is the bcc_B2/bcc_$D0_3$ transition line, T_C is the magnetic transition line, and T0 is the line where liquid and bcc_A2 have equal Gibbs free energy.

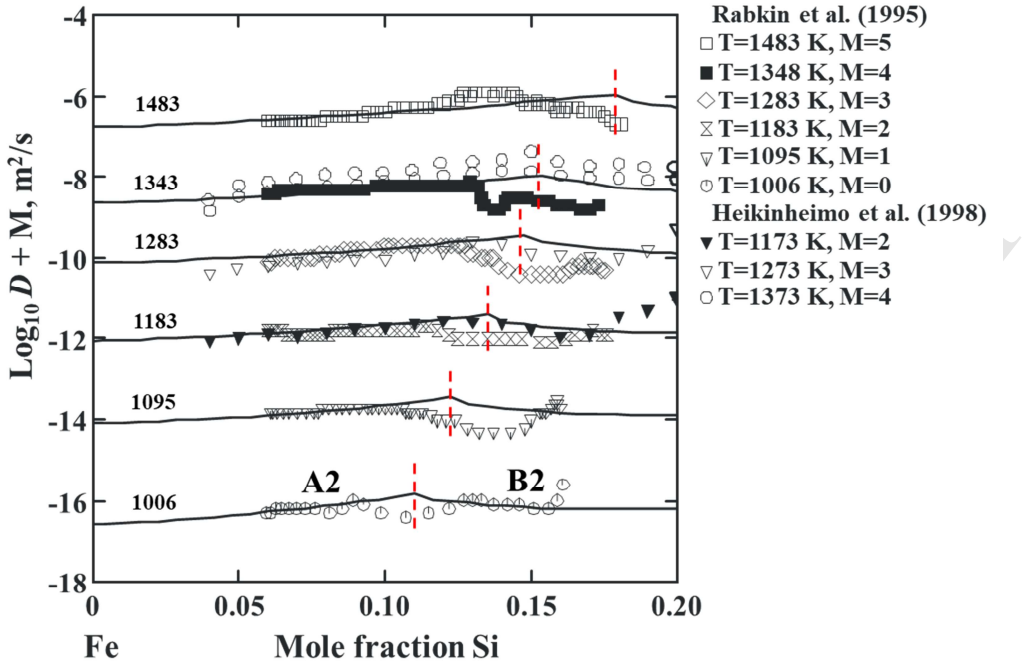

Fig. 3 Model-predicted interdiffusivities (solid lines) of Fe-Si solid solution along with the experimental data (symbols). A constant value of M was added to separate the data.

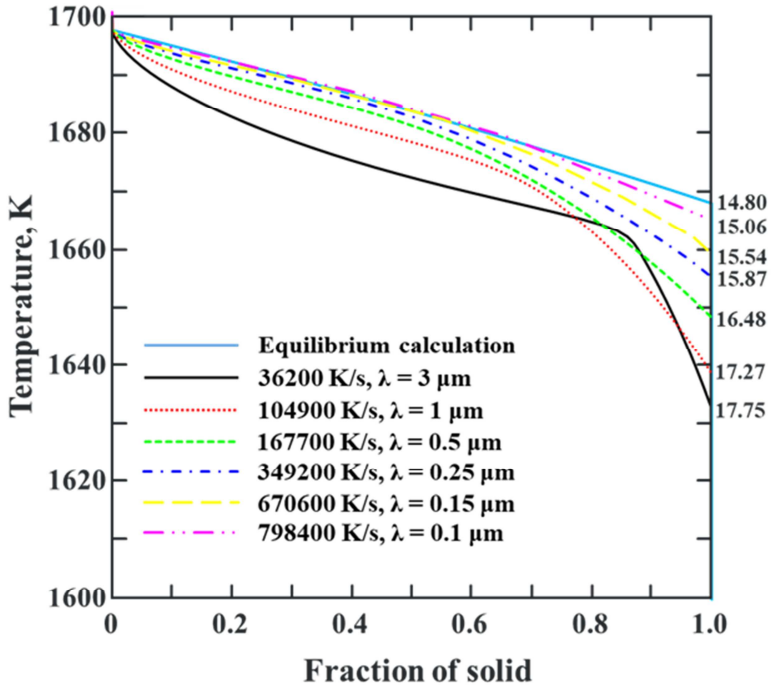

Fig. 4 Simulated solidification paths of Fe-6.5 wt.% Si under different cooling rates and half secondary dendrite arm spacings (λs).

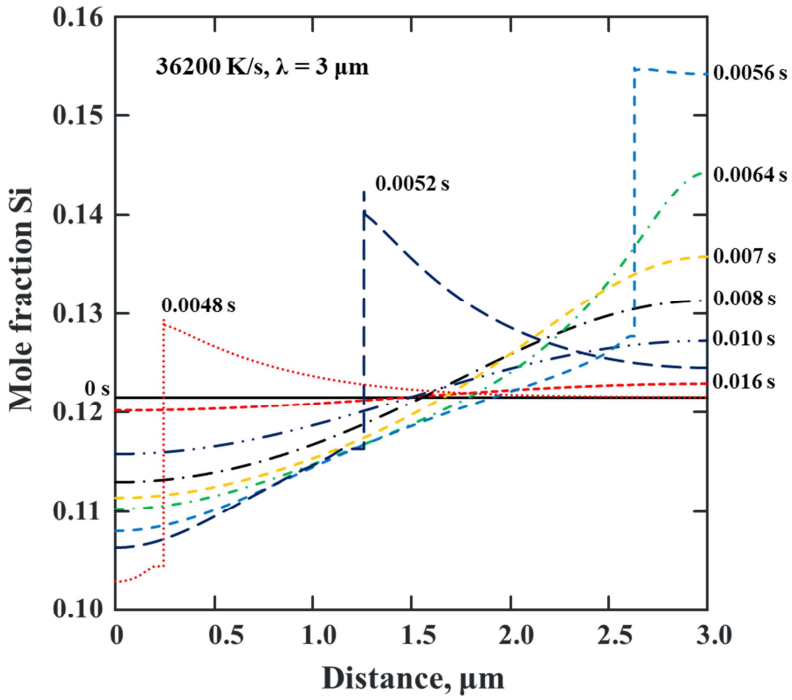

Fig. 5 Simulated time dependent concentration profiles along the half of secondary dendrite arm spacing of 3 μm in Fe-6.5 wt.% Si under a cooling rate of 36200 K/s.

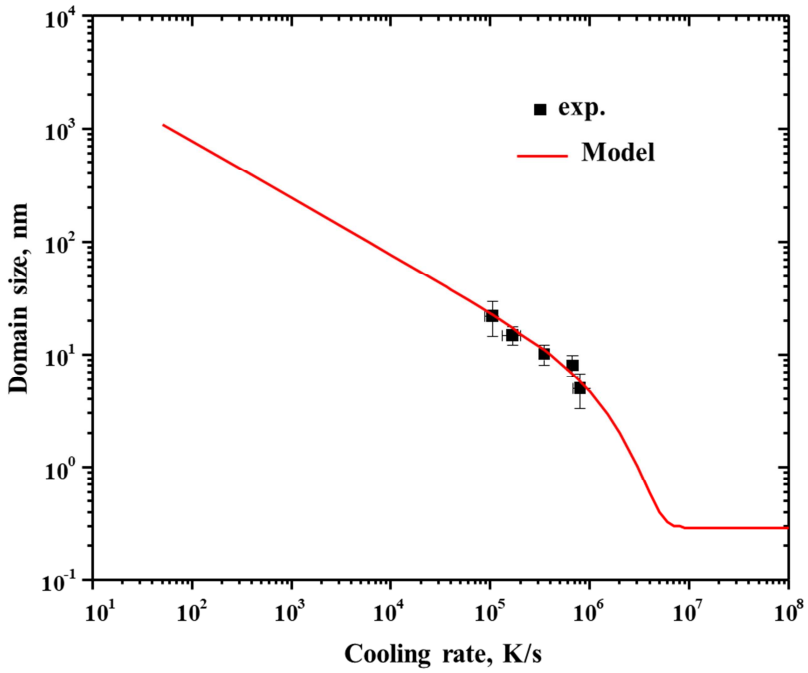

Fig. 6 Model-predicted domain size as a function of cooling rate along with the experimental data.

Highlights

- New Fe-6.5 wt.% Si melt spinning experiments and cooling rate measurements.
- The melt spun ribbons were characterized using TEM analysis.
- Solidification and solid-state transformation during rapid quenching were analyzed.
- The bcc_B2 domain growth was modeled using the Allen-Cahn theory.